

Article

Laser-Plasma Spectroscopy of Hydroxyl with Applications

Christian G. Parigger ^{1,*} , Christopher M. Helstern ¹, Benjamin S. Jordan ², David M. Surmick ³ 
and Robert Splinter ⁴ 

¹ Physics and Astronomy Department, University of Tennessee, University of Tennessee Space Institute, Center for Laser Applications, 411 B.H. Goethert Parkway, Tullahoma, TN 37388-9700, USA; chris.helstern@gmail.com

² Nuclear Engineering Department, Tickle College of Engineering, University of Tennessee, 1412 Circle Drive, Knoxville, TN 37912, USA; bjordan1@vols.utk.edu

³ Physics and Applied Physics Department, University of Massachusetts Lowell, Lowell, MA 01854, USA; David_Surmick@uml.edu

⁴ Wellingq Medical, Van der Waals Park 22, 9351 VC Leek, The Netherlands; rsplinter@gmail.com

* Correspondence: cparigge@tennessee.edu; Tel.: +1-(931)-841-5690

Received: 4 February 2020; Accepted: 20 February 2020; Published: 22 February 2020



Abstract: This article discusses laser-induced laboratory-air plasma measurements and analysis of hydroxyl (OH) ultraviolet spectra. The computations of the OH spectra utilize line strength data that were developed previously and that are now communicated for the first time. The line strengths have been utilized extensively in interpretation of recorded molecular emission spectra and have been well-tested in laser-induced fluorescence applications for the purpose of temperature inferences from recorded data. Moreover, new experiments with Q-switched laser pulses illustrate occurrence of molecular recombination spectra for time delays of the order of several dozen of microseconds after plasma initiation. The OH signals occur due to the natural humidity in laboratory air. Centrifugal stretching of the Franck-Condon factors and r-centroids are included in the process of determining the line strengths that are communicated as a Supplementary File. Laser spectroscopy applications of detailed OH computations include laser-induced plasma and combustion analyses, to name but two applications. This work also includes literature references that address various diagnosis applications.

Keywords: plasma diagnostics; molecular spectra; diatomic molecules; plasma spectroscopy; laser spectroscopy; laser-induced breakdown spectroscopy; optical emission spectroscopy; molecular excitation temperature; combustion analysis; astrophysical spectroscopy

1. Introduction

Practical applications of molecular spectroscopy include diagnosis of hydroxyl (OH) diatomic molecules in the study of laboratory plasma and chemical processes. This work communicates state-of-the-art OH line-strength data that were well-tested in laser-induced fluorescence and emission spectroscopy diagnoses. Laser spectroscopy [1–3] usually delivers information about the temporal- and spatial- distribution of species. Diagnosis usually utilizes methods that are frequently encountered in characterization of plasma [4]. This work also communicates aspects of laser spectroscopy of OH that include active interrogation with excitation from ground- or lower molecular states and levels, viz. laser-induced fluorescence (LIF), and passive analyses of excited molecular states or levels encoded in the emitted light from laser-induced plasma, viz. optical emission spectroscopy (OES). However, laser spectroscopy examples primarily focus on OES of the OH molecule and at standard ambient temperature and pressure (SATP) laboratory conditions.

Molecular recombination spectra are readily observed following optical breakdown in laboratory air. Emission signals from the OH molecule in the UV near 306 nm can be recognized in air breakdown for time delays of the order of 10 μ s after cessation of the laser pulse, but recorded data for the $\Delta v = 0$ OH bands indicate spectral interference with N₂ second positive bands [5,6]. For time delays of the order of 100 μ s, however, ultraviolet OH emissions of the $\Delta v = 0$ bands dominate in the range of 305 nm to 322 nm. Hydrocarbon combustion typically produces OH that can be measured with laser-induced fluorescence (LIF) and planar laser-induced fluorescence (PLIF) [7,8].

This work aims to (a) publish OH line strength data [9] that can be directly utilized with associated graphing and non-linear fitting programs [10] that include the Nelder-Mead temperature (NMT) program and the Boltzmann equilibrium spectroscopy program (BESP); (b) communicate new experimental investigations for the purpose of estimating both typical signal strength and time-delays for occurrence of hydroxyl spectra in laboratory laser-sparks; (c) summarize possible approaches for determination of OH concentrations with reference to local equilibrium conditions for a variety of plasma species; (d) illustrate typical fluid physics phenomena that can be initially explored by employing shadowgraph techniques; (e) comment on the set extensively LIF- and OES- tested OH line strength data with respect to alternate or perhaps historic approaches for computation of theory spectra, and (f) stimulate further fundamental analysis and comparisons with laboratory data.

Fundamental analysis includes investigations of differences in spectra for OH and OD isotopologues using the program LIFBASE [11]. Applications include laser ablation molecular isotopic spectrometry (LAMIS) [12]. Recent OH data-base developments [13] for predictions with PGOPHER [14] indicate the continued interest in establishing well-defined parameters for computation of OH spectra for analysis of diatomic molecule signatures, viz. hydroxyl, abundant in interstellar medium (ISM) along with other matter and radiation in the region between star systems. In that work, including exo-planet studies, the ExoMol data-base [15,16] is expected to assist in analysis of available superposition spectra.

2. Mini-Summary of OH Literature and Applications

The OH diatomic molecule occurs frequently as an intermittent molecule as part of a volley of chemical reactions that occur for example in plasma and that are measured in combustion processes. Examples of fundamental interests include exploration of the effects of chemical reactions on non-isothermal plasma [17] and the effect of N₂ and O₂ on OH production [18]. Related studies focus on line-by-line emission spectra from non-equilibrium plasma [19].

In another application, the OH radical has been employed for velocity mapping [20]. The hydroxyl group provides an attractive flow tracer, which includes the use of aldehydes in quantifying the air-fuel ratio in combustion chambers [21,22]. Furthermore, the use of laser-induced fluorescence yields high accuracy in determination of peroxy radicals [23]. The peroxide radical quantification process has particular applications in the determination of removal of pollutants, which are contributing to the oxidation of hydrocarbons. Furthermore, the reaction of peroxy radicals with nitrogen monoxide and -dioxide leads to the formation of ozone, a general environmental concern [23]. Laser-induced fluorescence can for instance be applied to quantify the presence of pollutants in the atmosphere, i.e., troposphere, based on the reactions with OH. The hydroxyl group containing radicals are the primary result of photolysis of ozone [23].

Measurement and tracking of OH levels in the tropospheric atmosphere is of critical importance owing to the fact that OH is the most important oxidant according to Wang because of its ability to remove trace gases [24]. Laser Induced Fluorescence has been used as the basis for a ground-based measuring system for tracking the OH levels in the tropospheric atmosphere and this ability will continue to be important and relevant to monitor the pollutants in the atmosphere [24]. Planar laser-induced fluorescence (PLIF) is one of the most widely used techniques for investigating flows of reactants such as OH [25]. Understanding of the temperatures of the reactants in flows has been a subject of recent investigation through the fitting of simulated OH excitations spectra [26,27].

These applications require continued deepened understanding of the behavior of OH plasma as offered in the research discussed in this article.

Additional literature on OH spectroscopy is rather exhaustive. This work however communicates a selected subset of papers that are of interest in hydroxyl diagnosis. In other words, various References are included to convey a mini-review of relevant literature that focuses on the OH diatomic molecule. Spectroscopic data for OH analysis are typically derived from Fourier transform spectroscopy [28,29] or by detailed studies of rotational spectra [30]. Fundamental data of OH molecular transitions are communicated in selected references [31–49]. Interrogations of ground-state or ground-level populations employ laser-induced fluorescence [50–68] with practical applications to combustion diagnosis [69–74]. However, diagnosis applications are based on extensive studies of the ultraviolet OH system [75–93].

3. Experimental Details

Standard experimental components are used for laser-induced breakdown spectroscopy, summarized previously, but are included for completeness, e.g., see reference [94] or for general laser-induced breakdown spectroscopy references [95,96]. The arrangement for the experiments reported in this work consists of a set of components typical for time-resolved, laser-induced optical emission spectroscopy, or nanosecond laser-induced breakdown spectroscopy (LIBS) [95]. Primary instrumentation includes a Q-switched neodymium-doped yttrium aluminum garnet, Nd:Y₃Al₅O₁₂ (Nd:YAG) device (Quantel model Q-smart 850, USA) operated at the fundamental wavelength of 1064-nm to produce full-width-at-half-maximum 6-ns laser radiation with an energy of up to 850 mJ per pulse, a laboratory type Czerny-Turner spectrometer (Jobin Yvon model HR 640, Fr) with a 0.64-m focal length and equipped with a 1200 grooves/mm grating, an intensified charge coupled device (Andor Technology model iStar DH334T-25U-03, USA) for recording of temporally and spatially resolved spectral data, electronic components for synchronization, and various optical elements for beam shaping, steering and focusing.

In previous experiments, captured shadowgraphs of the breakdown plasma [97] served the purpose of visualizing the plasma expansion when using 850 mJ, 6-ns radiation. The captured images are consistent with results of fluid-dynamic expansion phenomena [98] presented in the literature. In laser-ablation research, shockwave expansion studies [99] from a solid sample into air or into a gaseous environment such as argon are important for laser-induced breakdown spectroscopy (LIBS) that is applied for determination of elemental composition of the sample.

However, it is important to obtain shadowgraphs for plasma excitation energies that were employed for time-resolved spectroscopy. Shadowgraphs reported recently [94] are captured using two separate laser devices (Continuum Surelite model SL I-10, USA) that can be externally operated to deliver laser pulses with a well-defined time delay showing less than ± 1 ns trigger-jitter between the pulses. The experiments reported in reference [94] are extended to time delays of the order of 100 μ s for the purpose of visualizing the breakdown site for time delays that correspond to reasonable OH signals.

For visualization studies, both lasers are frequency-doubled to operate at the 2nd harmonic, 532-nm wavelength, and both beams are spatially overlapped. Both pulses can be delivered with a minimum time delay of 300 ns. Shadowgraphs are recorded by external synchronization of the Surelite and Quantel laser devices and by externally triggering the camera (Silicon Video 9C10 color camera, USA) that records the images that are projected onto a screen.

4. Results and Discussion

4.1. Shadowgraphs

Investigations of expanding laser-induced shockwaves and fluid-physics phenomena utilize effectively high shutter-speed shadowgraph photography. Figure 1 illustrates the essential experimental module that is composed of a focusing lens for generation of the optical breakdown plasma, and an

imaging lens that projects the interaction volume onto a screen. Two adjustable iris are employed for alignment. The iris on the laser side allows on to adjust the ratio of focal length, F , and of the beam diameter, D . For the shadowgraph studies reported in this work, a ratio of $F/D = f^\# = 20$ is used.



Figure 1. Module for recording shadowgraphs of optical breakdown in air. The collimated laser beam (red arrow) is focused with $f/20$ optics. The asterisk symbolically indicates optical breakdown. The interaction area is illuminated by a time-delayed laser beam (green arrow), and images are projected onto a screen (not shown) and recorded with a digital camera.

Figure 2a,b illustrate typical shadowgraphs recorded for time-delays of $54.25 \mu\text{s}$ and $104.25 \mu\text{s}$, respectively. The laser is incident from the right as indicated by the arrow in the single shot captured shadowgraph. While an outgoing shockwave occurs for time delays of the order of $1 \mu\text{s}$, as recently communicated in reference [94], Figure 2 depicts well developed vortices and fluid flow towards the incoming laser beam. In view of laser spectroscopy, a time-resolved data taken along a narrow slice along the horizontal direction would be affected by fluid dynamics.

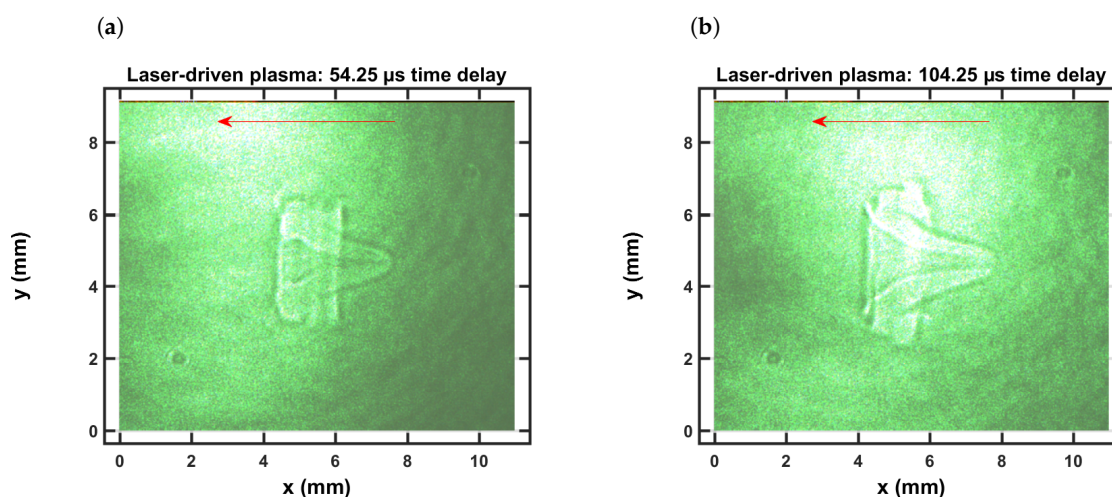


Figure 2. Single-shot shadowgraph of the expanding laser-induced plasma initiated with a 170-mJ, 6-ns, 1064-nm focused beam, and imaged using a 5-ns, 532-nm back-light that is time-delayed by (a) $54.25 \mu\text{s}$ and (b) $104.25 \mu\text{s}$.

4.2. Measurement of OH Spectra

Time-resolved spectroscopy of laser-induced plasma in laboratory air at a relative humidity level of 25% reveal characteristic ultraviolet OH data due to molecular recombination. The natural moisture present in the air causes occurrence of OH spectra. In thermodynamic equilibrium, the chemical composition of plasma is comprised of a volley of species. Figure 3 illustrates computed OH density versus temperature using the chemical equilibrium with applications (CEA) program [100,101].

For relative humidity in the range of 5% to 50%, the maximum OH signals are in the range of 3000 K to 3200 K. At a humidity level of 25% and at a temperature of 293.15 K (21 °C), air contains water at an amount of 4 g/kg_{dryair} [102], or 0.0114 mol/mol_{dryair} [102]. The dry air composition [103] and the H₂O content provide the input parameters for the CEA program [101] are listed in Table 1. Minor species such as carbon dioxide, helium, methane, krypton, hydrogen, xenon show mole-fractions below 2×10^{-5} and are not included in the computations, except hydrogen. The hydrogen mole fraction in dry air is of the order of 5×10^{-6} . This residual amount of hydrogen cannot cause the level of OH signals reported in this work. In fact, CEA results obtained with 50% relative humidity show 1000× larger maximum OH density (near 3200 K) than that for dry air (near 2200 K) containing a mole fraction of 5×10^{-6} hydrogen.

Table 1. Input values for computation of air species with the chemical equilibrium with applications (CEA)-code for 25% relative humidity. The sum of mole fractions are normalized to 1 in the code.

Species	Mole Fraction
nitrogen	0.78
oxygen	0.21
argon	0.00934
hydrogen	0.000005
water	0.01144

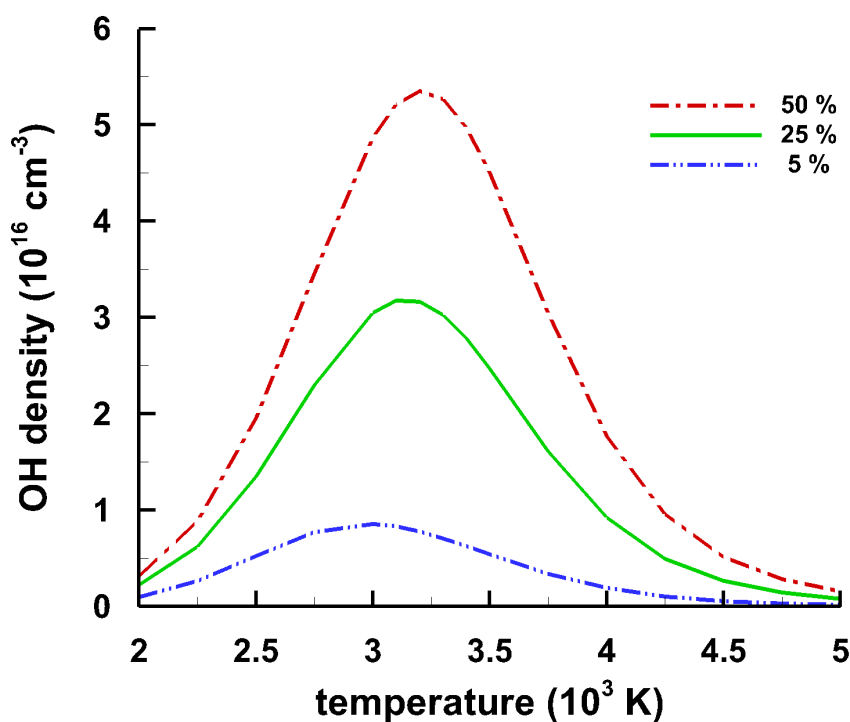


Figure 3. Calculated equilibrium hydroxyl (OH) density versus temperature. For air with 25% relative humidity, the OH density reaches a maximum of $\approx 3 \times 10^{16} \text{ cm}^{-3}$ at $T \approx 3.1 \text{ kK}$.

Optical breakdown was generated at a rate of 10 Hz, with the laser beam focused with $f/5$ optics from the top, or parallel to the slit, analogous to recently reported CN laser spectroscopy [94]. Figure 4 illustrates the experimental arrangement for imaging of the laser-plasma onto the vertical slit of the spectrometer. The laser beam, parallel to the slit, arrives from the top (red arrow) and is focused with $f/5$ -optics by an anti-reflection coated, 25.4-mm (1 in.) lens. The air-breakdown plasma, indicated by the asterisk is imaged 1:1 with a 50.8-mm lens.

The spot radius, ω_0 , for perfect Gaussian-beam focusing [104,105] amounts to

$$\omega_0 = \frac{2}{\pi} f^\# \lambda_{\text{laser}} . \quad (1)$$

With the wavelength, $\lambda_{\text{laser}} = 1064 \text{ nm}$, one finds $\omega_0 = 3.4 \text{ }\mu\text{m}$. However, spherical aberrations increase the spot-size. Computations of focal volume distributions are presented, for example, in references [6,9,12,106]. Moreover, optical breakdown can occur prior to reaching the focal spot predicted with Gaussian-beam focusing as irradiance-levels reach breakdown threshold [8]. In the experiments, the irradiance is of the order of $10\times$ more than that needed for optical breakdown in dry air.

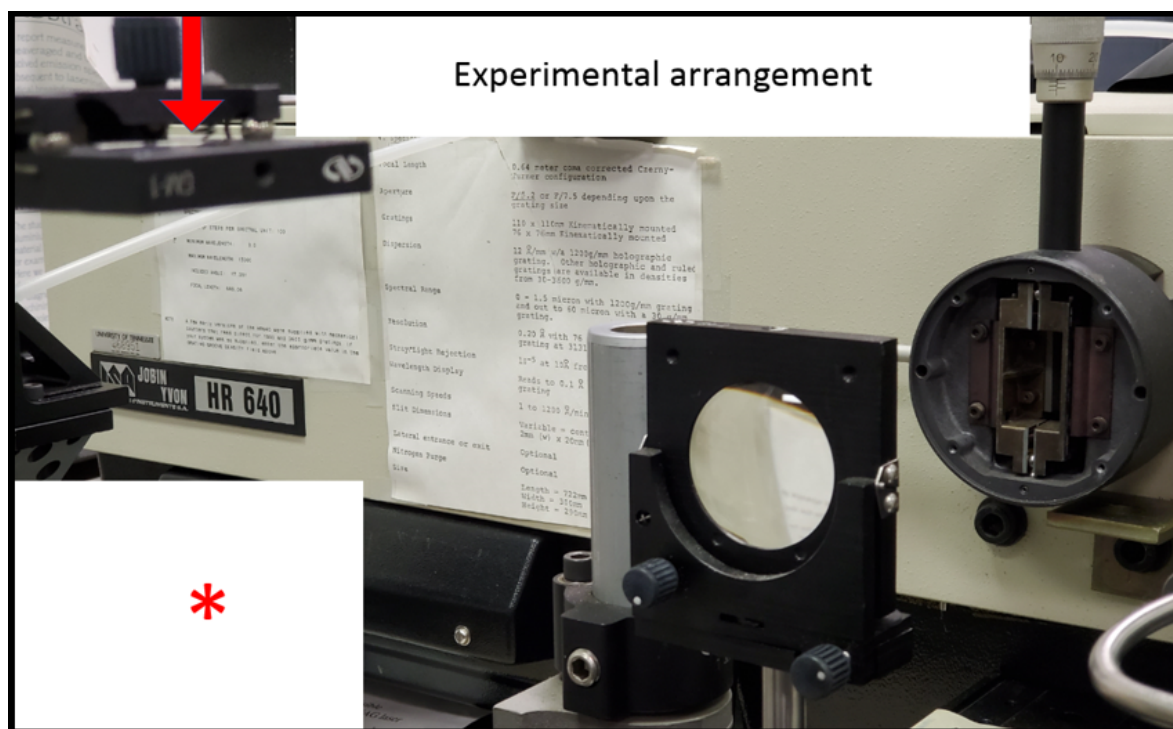


Figure 4. Experimental arrangement for time-resolved spectroscopy. The laser beam (red arrow) is focused to generate optical breakdown, indicated by the asterisk in the lower left of the photograph. The plasma is 1:1 images onto the slit of the spectrometer. Time-resolved data are recorded with an intensified charge-coupled device (not shown) positioned at the exit plane of the spectrometer.

The detector pixels are binned in 4-pixel tracks along the slit direction, resulting in obtaining 256 spectra for each time delay. Measurements comprise accumulation of 100 consecutive laser-plasma events for 11 separate time delays at $10 \text{ }\mu\text{s}$ steps. The selected series explores the plasma decay with specific attention to recognition of OH molecular data free from spectroscopic interference.

Figures 5 and 6 illustrate spatio-temporal spectra that were recorded along the line-of-sight. The slit-height corresponds to the x-direction in Figure 2 and the line-of-sight corresponds to direction of the back light used for capture of shadowgraphs. The images are individually scaled and pseudo-colored using a rainbow distribution.

The raw spectra in Figure 5 and the corresponding averages in Figure 6 are consistent with previously recorded spectra using a UV-enhanced, intensified linear-diode array [5,107]. Figure 6 shows the averages of the recorded counts. Early delay-time data were analyzed using classic laser spectroscopy, namely, addition of superimposed N₂ second positive and OH spectra. Moreover, a program designed for study of plasma torches was applied using chemical equilibrium. It is clear that a variety of species, including electrons, contribute to the measured spectra [5,6]. Investigations of information content and error propagation analysis reveals reasonable diagnosis capabilities of the line-of-sight analysis.

In view of the recorded shadowgraphs (see Figure 2), there appears to be well defined fluid physics phenomena including vortex formation and implosion of the shockwave-dominated expansions. The vortex is well developed and the implosion towards the laser device is recognizable in Figure 2 for time delays of approx. 50 and 100 μ s. The direction of the implosion is determined by slightly asymmetric energy absorption, in other words, by the direction of the laser-beam. The energy absorption causes slight asymmetries of shock waves for pulse energies of 160 to 200 mJ/pulse [5], and the expansion speeds are above hypersonic for time delays of approx. 0.5 μ s.

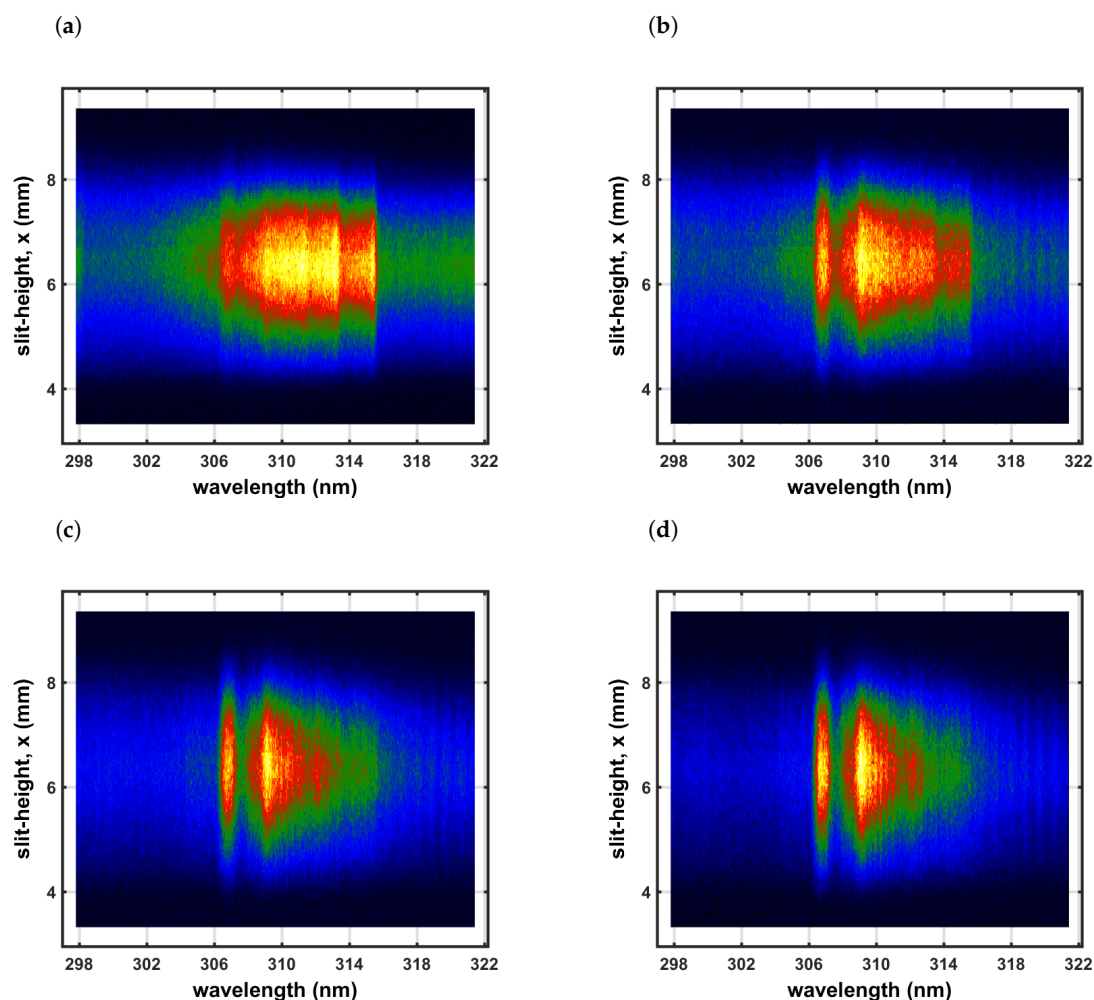


Figure 5. Recorded data of slit-height vs. wavelength. Gate width: 10 μ s, time delay (a) 20 μ s—primarily N₂ second positive spectra, (b) 30 μ s, (c) 40 μ s, and (d) 50 μ s—primarily OH spectra. Each displayed image is scaled from minimum to maximum and pseudo-colored using a rainbow distribution.

Table 2 conveys the shockwave radii for laser-induced plasma initiated with energies 200 mJ/pulse in standard ambient temperature and pressure (SATP) air. The table entries confirm that for 200-mJ/pulse the shockwave is outside the vertical dimension of the available slit of approx. 14-mm

height for 1:1 imaging. The shockwave radii were calculated using Taylor-Sedov model, analogous to recently published investigation of CN spectra [94],

$$R(\tau) = \left(\frac{E}{\rho} \tau^2 \right)^{1/5}. \quad (2)$$

The shockwave radius, $R(\tau)$, is a function of absorbed pulse energy, E , density of the gas, ρ , and time delay, τ .

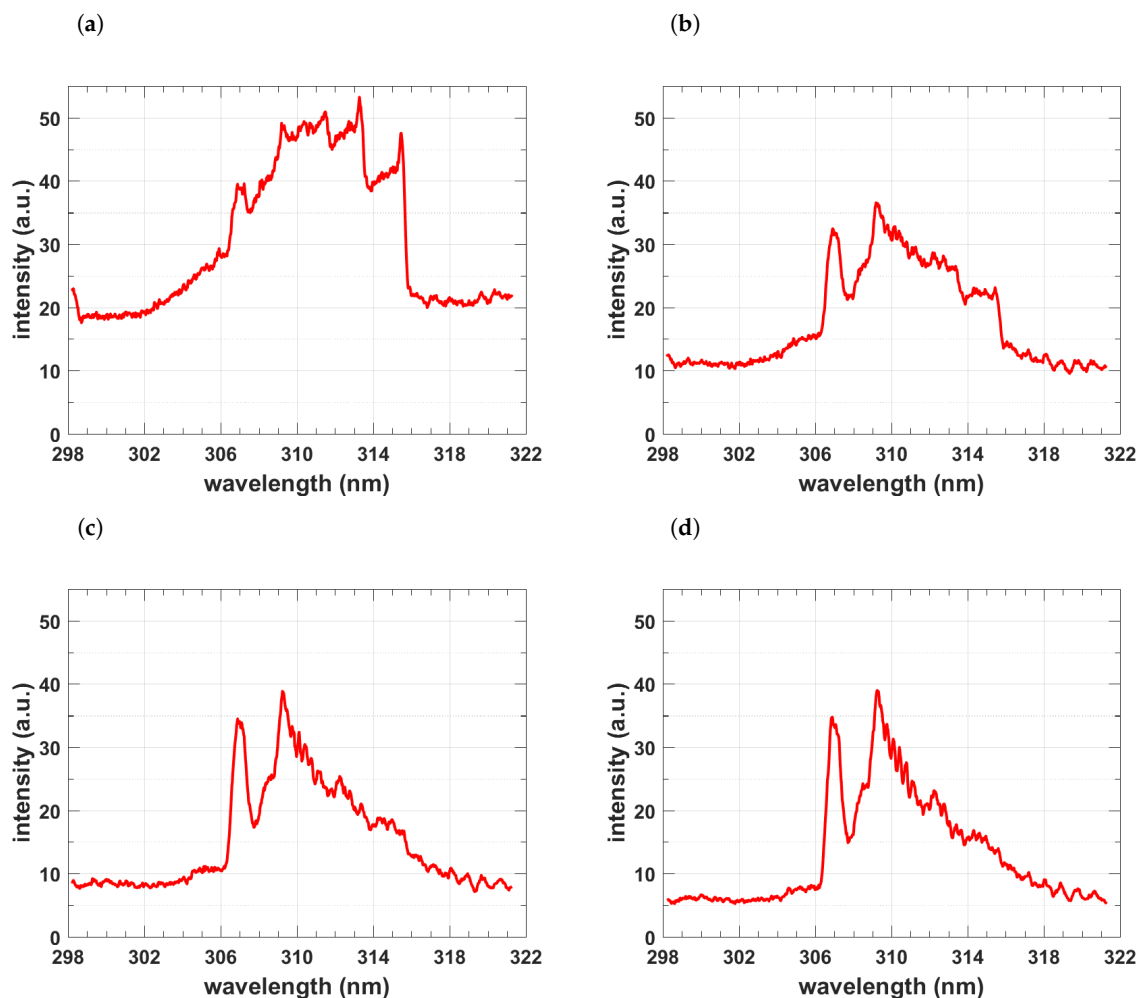


Figure 6. Average of spectra between 4.2 and 8.2 mm of Figure 5. Gate width: 10 μ s, time delay (a) 20 μ s—primarily N_2 second positive spectra (b) 30 μ s, (c) 40 μ s, and (d) 50 μ s—primarily OH spectra. Contributions from the N_2 second positive system diminish with increase of time delays.

Table 2. Computed shockwave radii for standard ambient temperature and pressure (SATP) air, 200 mJ energy/pulse.

Time Delay (μ s)	R (mm) for Air [$\rho = 1.2 \text{ kg/m}^3$]
20	9.21
25	10.1
50	13.3
75	15.7
100	17.5

4.3. Computation of OH Spectra

The computation of OH diatomic molecular spectra is based on collection of line-strength data [9] and application of algorithms for comparison of measured and computed spectra [10]. Figure 7 illustrates computed OH data for spectral resolutions of 0.25 nm and 0.0025 nm that correspond to typical resolutions in laser-induced spectroscopy with intensified array detectors and nominal pico-meter resolution stick-spectra. The line-strength data are included as a Supplement, and Appendix A reports typical fitting results of well-calibrated data [5] in terms of wavelength and instrument sensitivity.

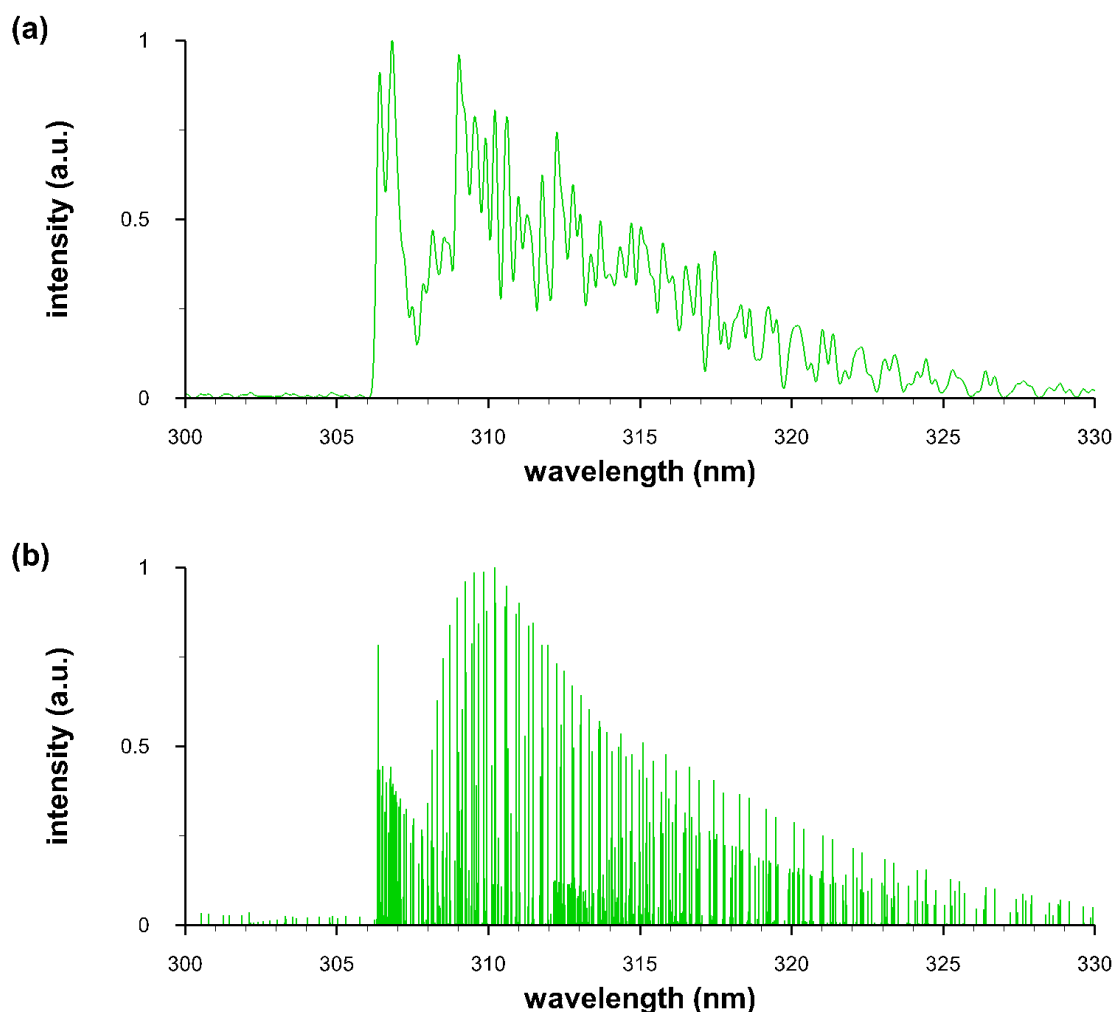


Figure 7. Computed spectra: $T = 6000$ K; spectral resolution (a) 0.25 nm and (b) 0.0025 nm.

4.4. Comparisons of Recorded and Computed OH Spectra

The accuracy of the line strength data can be evaluated by comparing predictions with optical emission spectroscopy (OES) and laser induced fluorescence (LIF) records. Line strength wavelengths are accurate to better than 0.05 cm^{-1} or better than 0.5 pm at a wavelength of 300 nm. In passive emission spectroscopy, small variations in the precision of the computed spectral data can add up to differences in predicted and measured data although laser-plasma spectral resolutions are frequently of the order of 0.1 nm, in other words, the line strength wavelengths are known about a factor of 200 better than available in OES. In addition, the predicted relative magnitudes of individual lines within a band system need to agree as well.

The hydroxyl $A^2\Sigma^+ \leftrightarrow X^2\Pi_i$ ultraviolet system line strengths (see Appendix A) contain 0-0, 0-1, 1-0, 1-1, 1-2, 2-0, 2-1, 2-2, and 2-3 bands. Centrifugal stretching of the Franck-Condon factors and r-centroids are included in the process of determining the line strengths. Figures 8 and 9 illustrate laser induced fluorescence and optical emission spectroscopy comparisons. The specific details of the LIF and OES experiments conducted for measurement results included in Figures 8 and 9 are not described in detail, important are demonstrations of the line-strength data accuracy and OH diatomic molecular band appearances. Figure 9 also shows contributions from the different bands of the $\Delta v = 0$ OH transitions.

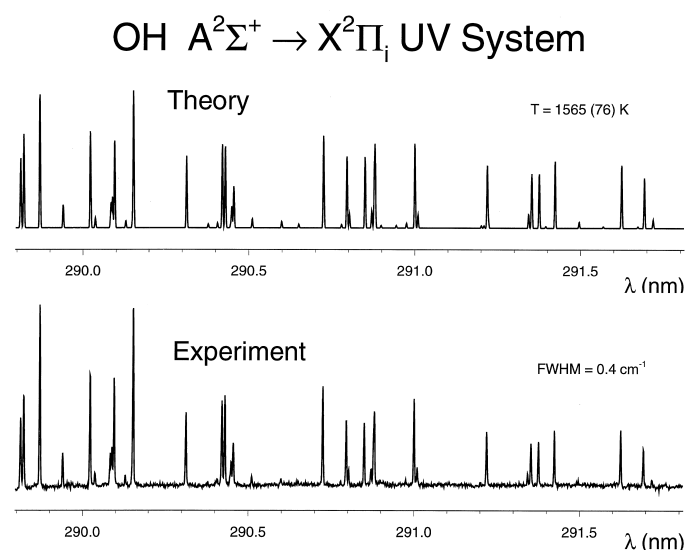


Figure 8. Comparisons of measured and recorded laser induced fluorescence spectra [108].

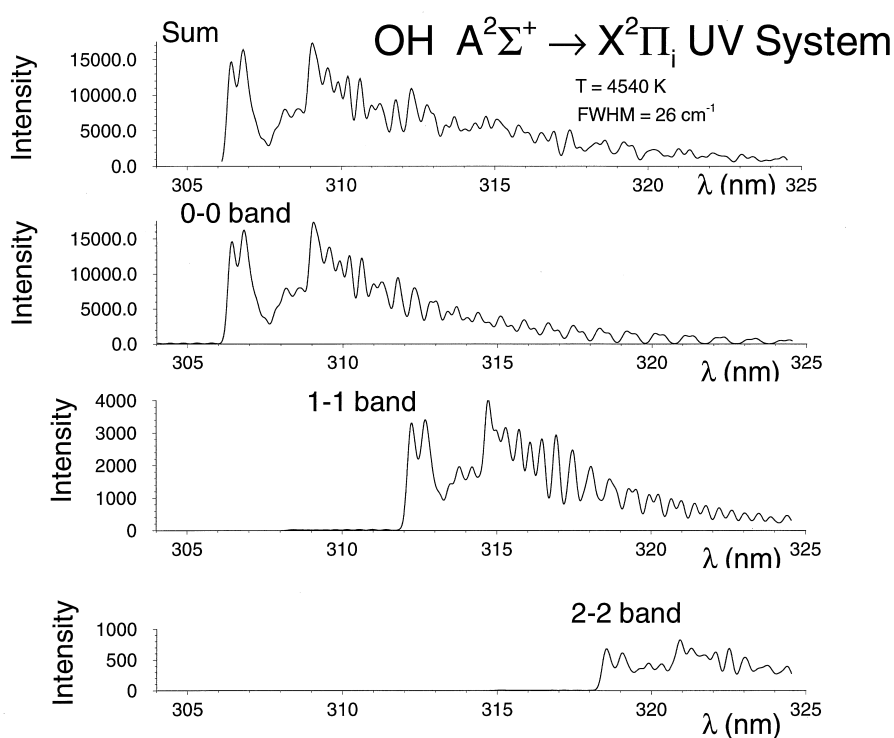


Figure 9. Comparisons of measured and recorded laser-plasma emission spectroscopy [108].

4.5. Temperature and Density of OH

The temperature is inferred from the OH spectra by fitting measured with computed molecular spectra. The procedure, program and a example result are included in the Appendix A. In this work, an average temperature is obtained from the line-of-sight data assuming an equilibrium plasma excitation temperature. This particular assumption has been investigated by employing predictions from chemical equilibrium codes as input to a general non-equilibrium air radiation program [5,6]. Various species densities are predicted within the equilibrium assumption, and include OH, Ar, N, O, e⁻, N₂, O₂, CO, NO, NO⁺ (see Table 1 in Reference [5]). For laboratory air, the OH concentration maximum occurs at temperatures of approx. 3000 K at a time delay of approx. 100 μs and are of the order of 10¹⁶ cm⁻³. A detailed study [5] used linear diode arrays and employed up to 100 Hz repetition rate from a Nd:YAG laser device (Coherent Infinity 40-100, USA). Determination of OH temperature and molecular species concentrations in laser-induced laboratory air breakdown includes Monte Carlo simulation as well for estimation of error bars [5]. Contributions from species other than OH for time delays of the order of 100 μs can be calculated using a general non-equilibrium program in the equilibrium mode, with inputs obtained from chemical equilibrium codes - one finds approx. 5% wavelength-dependent peak-background contributions from species other than OH [108,109].

In view of the shadowgraphs reported in this work (see Figure 2), averages of well-developed fluid physics phenomena were recorded with linear diode arrays, viz. summing along the slit-height. It would appear reasonable to determine an association of spatially resolved spectra with the recorded expansion. However, simultaneous recording of shadowgraphs and spectra would be necessary for establishment of expansion characteristics following laser-induced breakdown in air. Such an association of shadowgraphs for time-delays of the order of 1 μs has been reported recently using CN emission spectroscopy [94]. Radon inverse transforms or computed tomography would appear necessary, but possibly Abel inverse transforms may be sufficient as one realizes the symmetry of the vortex indicated in Figure 2.

5. Conclusions

This work illustrated analysis of recorded time-resolved OH spectra using accurate line strength files. Presence of the hydroxyl radical is usually associated with combustion, however in laboratory air that contains residual moisture, OH emissions occur as a result of recombination radiation. Laser-plasma and laser-induced fluorescence measurements indicate the accuracy of the OH line strength data that are made publicly available for the first time in this publication. Hydroxyl ultraviolet system line strengths complement those for aluminum monoxide, cyanide, diatomic carbon, and titanium monoxide already available for selected electronic transitions. Future work should address association of OH signals with spatial variations due to vortex-formation and implosions that can be visualized by employing effectively high shutter-speed shadowgraph photography that is only limited by the pulse-width of the back light. The presented work is applicable to electrical-spark analytical chemistry. Moreover, comparisons of PGOPHER and of the nonlinear NMT predictions should be content of future research, including comparisons with LIFBASE predictions. These comparisons are expected to lead to further insights in the analysis of laboratory laser-plasma and on an astronomical scale help advancements in exo-planet and interstellar-medium research.

Supplementary Materials: The Supplementary Files are available online.

Author Contributions: All authors contributed equally to this work. All authors have read and agreed to the published version of the manuscript.

Funding: This research received no external funding.

Acknowledgments: The authors wish to acknowledge the support in part by the Center for Laser Applications at the University of Tennessee Space Institute.

Conflicts of Interest: The authors declare no conflict of interest.

Appendix A. Hydroxyl Line Strengths

Appendix A.1. Overview

The appendix communicates the hydroxyl line strengths for fitting of measured and computed spectra for the OH ultraviolet bands. The line-strength data for the ultraviolet system of OH are attached in a Supplementary File, *OHuv-lsf.txt*. The details for the establishment of the line-strength data are communicated in the recently published book on diatomic molecular spectroscopy [9]. The line strength data can be utilized together with the previously published Nelder-Mead temperature (NMT) and Boltzman equilibrium spectroscopic temperature (BESP) [10] programs along with descriptions of how to use it. In other words, ultraviolet OH line strengths are added to the files for CN, AlO, C₂, and TiO [10].

Appendix A.2. Example Data File and Fitted Spectra

This section summarizes typical fitting steps, and it includes recorded and fitted data for spectra presented in Section 4. The fitting routine has been applied previously laser-induced spectroscopy [5]. Hydroxyl recombination spectra occur subsequent to laser-induced optical breakdown in laboratory air. The analysis and interpretation of OH emission spectra is discussed in view of chemical equilibrium predictions [5]. Figure A1 shows recorded and re-fitted OH spectra together with the residual- or difference-spectrum.

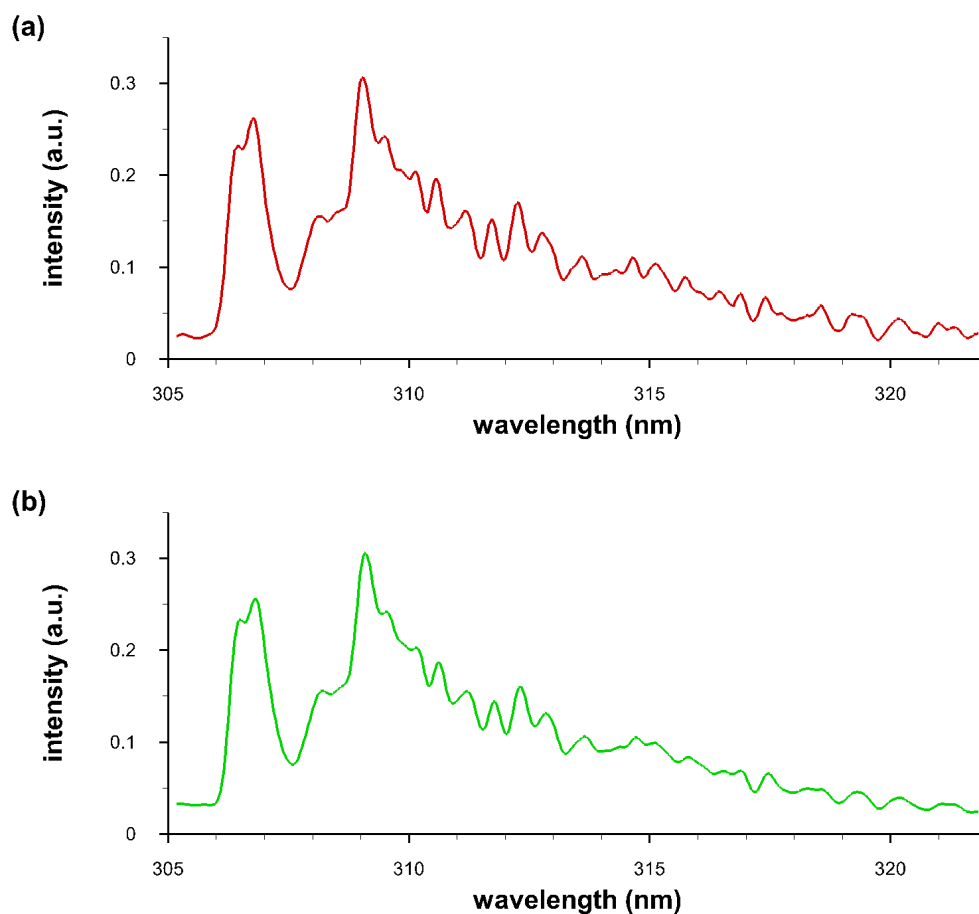


Figure A1. Cont.

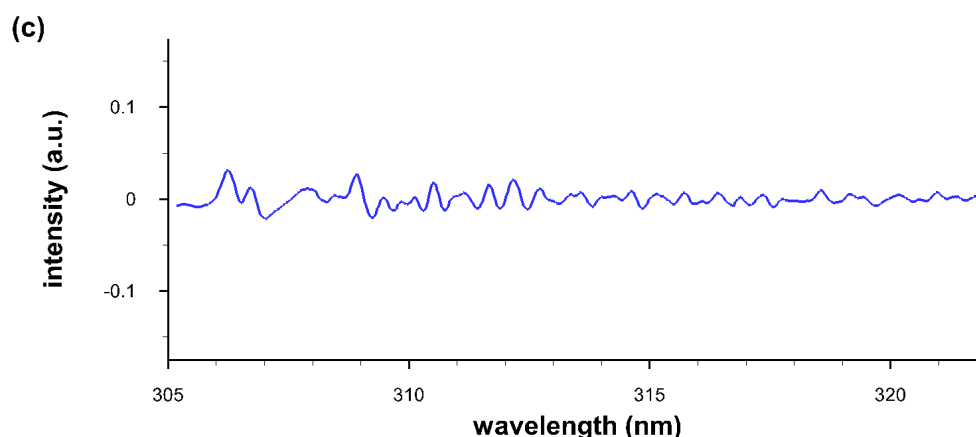


Figure A1. (a) Recorded and (b) fitted OH spectra. (c) Difference of measured and of fitted spectra. Time delay: 100 μ s, gate width: 50 μ s, temperature: 3470 K.

The recorded and fitted data set comprised of 512 points of recorded signal versus calibrated wavelength are included as Supplementary Files “OH100micros.dat” and “OH100micros-fit.txt”. The fitting results utilize a second-order polynomial for fitting background variation, temperature, and spectral line width. The inferred temperature equals $T = 3470$ K and the fitted line width, $\Delta\lambda$, equals $\Delta\lambda = 0.36$ nm.

References

1. Kunze, H.-J. *Introduction to Plasma Spectroscopy*; Springer: Heidelberg, Germany, 2009.
2. Fujimoto, T. *Plasma Spectroscopy*; Clarendon Press: Oxford, UK, 2004.
3. Ochkin, V.N. *Spectroscopy of Low Temperature Plasma*; Wiley-VCH: Weinheim, Germany, 2009.
4. Boulos, M.I.; Fauchais, P.; Pfender E. *Thermal Plasmas. Fundamentals and Applications*; Plenum Press: London, UK, 1994.
5. Parigger, C.G.; Guan, G.; Hornkohl, J.O. Measurement and analysis of OH emission spectra following laser-induced optical breakdown in air. *Appl. Opt.* **2003**, *42*, 5986–5991. [[CrossRef](#)]
6. Parigger, C.G. Laser-induced breakdown in gases: Experiments and simulation. In *Laser Induced Breakdown Spectroscopy (LIBS): Fundamentals and Applications*; Miziolek, A.W., Palleschi, V., Schechter, I., Eds.; Cambridge Univ. Press: New York, NY, USA, 2006; pp. 171–193.
7. Chen Y.-L.; Lewis, J.W.L. Visualization of laser-induced breakdown and ignition. *Opt. Express* **2001**, *9*, 360–372. [[CrossRef](#)] [[PubMed](#)]
8. Qin, W.; Chen, Y.-L.; Lewis, J.W.L. Time-resolved temperature images of laser-ignition using OH two-line laser-induced fluorescence (LIF) thermometry. *Int. Flame Res. Found. Combust. J.* **2005**, *8*, 200508.
9. Parigger, C.G.; Hornkohl, J.O. *Quantum Mechanics of the Diatomic Molecule with Applications*; IOP Publishing: Bristol, UK, 2019.
10. Parigger, C.G.; Woods, A.C.; Surmick, D.M.; Gautam, G.; Witte, M.J.; Hornkohl, J.O. Computation of diatomic molecular spectra for selected transitions of aluminum monoxide, cyanide, diatomic carbon, and titanium monoxide. *Spectrochim. Acta Part B At. Spectrosc.* **2015**, *107*, 132–138. [[CrossRef](#)]
11. Luque, L.; Crosley, D.R. LIFBASE: Database and Spectral Simulation for Diatomic Molecules (Version 2.1.1). 2013. Available online: <https://www.sri.com/cem/lifbase> (accessed on 3 September 2019).
12. Parigger, C.G.; Surmick, D.M.; Helstern, C.M.; Gautam G.; Bol’shakov, A.A. Molecular Laser-Induced Breakdown Spectroscopy. In *Laser Induced Breakdown Spectroscopy*, 2nd ed.; Singh, J.P., Thakur, S.N., Eds.; Elsevier: New York, NY, USA; Amsterdam, The Netherlands, 2020; Chapter 7.
13. Yousefi, M.; Bernath P.F.; Hodges, J.; Masseron, T. A new line list for the $A^2\Sigma^+ - X^2\Pi$ electronic transition of OH. *J. Quant. Spectrosc. Radiat. Transf.* **2018**, *217*, 416–424. [[CrossRef](#)]
14. Western, C.M. PGOPHER: A program for simulating rotational, vibrational and electronic spectra. *J. Quant. Spectrosc. Radiat. Transf.* **2017**, *186*, 221–242. [[CrossRef](#)]

15. Tennyson, J. The ExoMol Project: Molecular Opacity Calculations at University College London, Workshop on Astrophysical Opacities. In *Astronomical Society of the Pacific (ASP) Conference Series 515, Michigan University, Kalamazoo, MI, USA, 1–4 August 2017*; Mendoza, C., Sylva, T.-C., Colgan, J., Eds.; Astronomical Society of the Pacific: San Francisco, CA, USA, 2018; Volume 137.
16. Tennyson, J.; Yurchenko, S.N.; Al-Refaie, A.F.; Barton, E.J.; Chubb, K.L.; Coles, P.A.; Diamantopoulou, S.; Gorman, M.N.; Hill, C.; Lam, A.Z.; et al. The ExoMol database: Molecular line lists for exoplanet and other hot atmospheres. *arXiv* **2018**, arXiv:1603.05890.
17. Chernyak, V.Y.; Nedybaliuk, O.A.; Martysh, E.V.; Iukhymenko, V.V.; Prysiazhnevych, I.Y.; Solomenko, O.V.; Veremii, I.P.; Shevchenko, T. Low temperature plasma and plasma technologies: Plasma catalysis of chemical reactions. *Prob. At. Sci. Technol. Ser. Plasma Phys.* **2014**, *6*, 124–129.
18. Srivastava, N.; Wang, C.J. Effect of N₂ and O₂ on OH radical production in an atmospheric helium microwave plasma jet. *Plasma Sci. Technol.* **2019**, *21*, 115401. [[CrossRef](#)]
19. Vorač, J.; Synek, P.; Procházka, V.; Hoder, T. State-by-state emission spectra fitting for non-equilibrium plasmas: OH spectra of surface barrier discharge at argon/water interface. *J. Phys. D Appl. Phys.* **2017**, *50*, 294002. [[CrossRef](#)]
20. Ribarov, L.A.; Hu, S.; Wehrmeyer, J.A.; Pitz, W. Hydroxyl tagging velocimetry method optimization: signal intensity and spectroscopy. *Appl. Opt.* **2005**, *44*, 6616–6626. [[CrossRef](#)] [[PubMed](#)]
21. Itoh, T.; Kakuho, A.; Hishinuma, H.; Urushihara, T.; Takagi, Y.; Horie, K.; Asano, M.; Ogata, E.; Yamasita, T. Development of a New Compound Fuel and Fluorescent Tracer Combination for Use with Laser Induced Fluorescence. Society of Automotive Engineering (SAE) transactions. *Int. J. Engine Res.* **1995**, *104*, 2287–2300. [[CrossRef](#)] [[PubMed](#)]
22. Ahmed, A.M.; Mancarella, S.; Desgroux, P.; Gasnot, L.; Pauwels, J.-F.; El Bakali, A. Experimental and numerical study on rich methane/hydrogen/air laminar premixed flames at atmospheric pressure: Effect of hydrogen addition to fuel on soot gaseous precursors. *Int. J. Hydrogen Energy* **2016**, *41*, 6929–6942.
23. Fuchs, H. *Measurement of Peroxy Radicals Using Laser-Induced Fluorescence Technique*; Forschungszentrum Jülich GmbH, Environment: Jülich, Germany, 2006; Volume 72. [[CrossRef](#)]
24. Wang, F.; Hu, R.; Chen, H.; Xie, O.; Wang, Y.; Li, Z.; Jin, H.; Liu, J.; Liu, W. Development of a field system for measurement of tropospheric OH radical using laser-induced fluorescence technique. *Opt. Express* **2019**, *27*, A419–A435.
25. Wang, Y.; Jain, A.; Kulatilaka, W. Hydroxyl radical planar imaging in flames using femtosecond laser pulses. *Appl. Phys. B Lasers Opt.* **2019**, *125*, 90. [[CrossRef](#)]
26. Malmqvist, E.; Jonsson, M.; Larsson, K.; Alden, M.; Bood, J. Two-dimensional OH-thermometry in reacting flows using photofragmentation laser-induced fluorescence. *Combust. Flame* **2016**, *196*, 297–306. [[CrossRef](#)]
27. Kiefer, J.; Meyerhoefer, A.; Seeger, T.; Leipertz, A.; Li, Z.S.; Aldén, M. OH-thermometry using laser polarization spectroscopy and laser-induced fluorescence spectroscopy in the OH A-X (1,0) band. *J. Raman Spectrosc.* **2009**, *40*, 828–835. [[CrossRef](#)]
28. Abrams, M.C.; Davis, S.P.; Rao, M.L.P.; Engleman, R., Jr.; Brault, J.W. High-resolution Fourier transform spectroscopy of the Meinel system of OH. *Astrophys. J. Suppl. Ser.* **1994**, *93*, 351–395. [[CrossRef](#)]
29. Stark, G.; Brault, J.W.; Abrahms, M.C. Fourier-transform spectra of the A²Σ⁺ - X²Π Δv = 0 bands of OH and OD. *J. Opt. Soc. Am. B Opt. Phys.* **1994**, *11*, 3–32. [[CrossRef](#)]
30. Varberg, T. D.; Evenson, K.M. The rotational spectrum of OH in the v = 0-3 levels of its ground-state. *J. Mol. Spectrosc.* **1993**, *157*, 55–67. [[CrossRef](#)]
31. Becker, K.H.; Haaks, D.; Tatarczyk, T. The Natural lifetime of OH (²Σ⁺, v = 0, N = 2, J = 32) and its quenching by atomic hydrogen. *Chem. Phys. Lett.* **1974**, *25*, 564–567. [[CrossRef](#)]
32. Brockhinke, A.; Lenhard, U.; Bülter, A.; Kohse-Höinghaus, K. Energy transfer in the OH A²Σ⁺ state: The role of polarization and of multi-quantum energy transfer. *Phys. Chem. Chem. Phys.* **2005**, *7*, 874–881. [[CrossRef](#)]
33. Brophy, J.H.; Silver, J.A.; Kinsey, J.L. Direct measurement of the radiative lifetime of the A²Σ⁺ (v' = 0, K' = 1, J' = 32) state of OH and OD. *Chem. Phys. Lett.* **1974**, *28*, 418–421. [[CrossRef](#)] [[PubMed](#)]
34. Burris, J.; Butler, J.J.; McGee, T.J.; Heaps, W.S. Collisional deactivation rates for A²Σ⁺ (v' = 1) state of OH. *Chem. Phys.* **1988**, *124*, 251–258. [[CrossRef](#)]
35. Cattolica, R.J.; Mataga, T.G. Rotational-level-dependent quenching of OH A²Σ⁺ (v' = 1) by collisions with H₂O in a low-pressure flame. *Chem. Phys. Lett.* **1991**, *182*, 623–631. [[CrossRef](#)]

36. Cleveland, C.B.; Wiesenfeld, J.R. Electronic quenching of highly rotationally excited OH ($A^2\Sigma^+, v' = 0, 1$) by H_2O . *Chem. Phys. Lett.* **1988**, *144*, 479–485. [[CrossRef](#)]
37. Copeland, R.A.; Chalamala, B.R.; Coxon, J.A. Laser-Induced Fluorescence of the $B^2\Sigma^+ - X^2\Pi$ System of OH: Molecular constants for the $B^2\Sigma^+ (v = 0, 1)$ and $X^2\Pi (v = 7 - 9, 11 - 3)$. *J. Mol. Spectrosc.* **1993**, *161*, 243–252. [[CrossRef](#)]
38. Copeland, R.A.; Wiese, M.L.; Crosley, D.R. Vibrational-Energy transfer and quenching of OH ($A^2\Sigma^+, v' = 1$). *J. Phys. Chem.* **1988**, *92*, 5710–5715. [[CrossRef](#)]
39. Crosley, D. R.; Lengel, R.K. Relative transition-probabilities and electronic-transition moment in A-X system of OH. *J. Quant. Spectrosc. Radiat. Transfer* **1975**, *15*, 579–591. [[CrossRef](#)]
40. Derro, E.L.; Pollack, I.B.; Dempsey, L.P.; Greenslade, M.F.; Lei, Y.; Radenović, D.Ć.; Lester, M.I. Fluorescence-dip infrared spectroscopy and predissociation dynamics of OH $A^2\Sigma^+ (v = 4)$ radicals. *J. Chem. Phys.* **2005**, *122*, 244313. [[CrossRef](#)]
41. German, K.R. Direct measurement of radiative lifetime of $A^2\Sigma^+ (v' = 0)$ states of OH and OD. *J. Chem. Phys.* **1975**, *62*, 2584–2587. [[CrossRef](#)]
42. German, K.R. Collision and quenching cross-sections in $A^2\Sigma^+$ state of OH and OD. *J. Chem. Phys.* **1976**, *64*, 4065–4068. [[CrossRef](#)]
43. Hogan, P.; Davis, D.D. Comments on “Electronic quenching and vibrational-relaxation of OH ($A^2\Sigma^+ v' = 1$) state”. *J. Chem. Phys.* **1976**, *64*, 3901. [[CrossRef](#)]
44. Hogan, P.; Davis, D.D. Electronic quenching and vibrational-relaxation of OH ($A^2\Sigma^+ v' = 1$) state. *J. Chem. Phys.* **1975**, *62*, 4574–4576. [[CrossRef](#)]
45. Huber, K.P.; Holland, F.; Coxon, J.A. Jet emission-spectroscopy of OH and OD near 1850-A—1st observation of $A^2\Pi - ^2\Pi$ electronic-transition of OD. *J. Chem. Phys.* **1992**, *96*, 1005–1015. [[CrossRef](#)]
46. Jorg, A.; Esposito, D.; Werner, H.J. Rotational energy-transfer in OH ($A^2\Sigma^+, v' = 0$)—A method for the direct determination of state-to-state transfer-coefficients. *J. Chem. Phys.* **1990**, *93*, 6453–6462. [[CrossRef](#)]
47. Kienle, R.; Li, M.P.; Kohse-Höinghaus, K. A detailed rate equation model for the simulation of energy transfer in OH laser-induced fluorescence. *Appl. Phys. B Lasers Opt.* **1996**, *62*, 583–599. [[CrossRef](#)]
48. McDermid, I.S.; Laudenslager, J.B. Radiative lifetime and quenching rate coefficients for directly excited rotational levels of OH ($A^2\Sigma^+, v = 0$). *J. Chem. Phys.* **1982**, *76*, 1824–1831. [[CrossRef](#)]
49. Rahmann, U.; Kreutner, W.; Kohse-Höinghaus, K. Rate-equation modeling of single- and multiple-quantum vibrational energy transfer of OH ($A^2\Sigma^+, v' = 0$ to 3). *Appl. Phys. B Lasers Opt.* **1999**, *69*, 61–70. [[CrossRef](#)]
50. Bormann, F.C.; Nielsen, T.; Burrows, M.; Andresen, P. Single-pulse collision-insensitive picosecond planar laser-induced fluorescence of OH $A^2\Sigma^+ (v' = 2)$ in atmospheric-pressure flames. *Appl. Phys. B Lasers Opt.* **1996**, *62*, 601–607. [[CrossRef](#)]
51. Bormann, F.C.; Nielsen, T.; Burrows, M.; Andresen, P. Picosecond planar laser-induced fluorescence measurements of OH $A^2\Sigma^+ (v' = 2)$ lifetime and energy transfer in atmospheric pressure flames. *Appl. Opt.* **1997**, *36*, 6129–6140. [[CrossRef](#)]
52. Brockhinke, A.; Kreutner, W.; Rahmann, U.; Kohse-Höinghaus, K.; Settersten, T.B.; Linne, M.A. Time-, wavelength-, and polarization-resolved measurements of OH ($A^2\Sigma^+$) picosecond laser-induced fluorescence in atmospheric- pressure flames. *Appl. Phys. B Lasers Opt.* **1999**, *69*, 477–485. [[CrossRef](#)]
53. Brophy, J.H.; Silver, J.A.; Kinsey, J.L. Vibrationally excited OH from the reaction of H with NO_2 observed by laser-induced fluorescence. *J. Chem. Phys.* **1975**, *62*, 3820–3822. [[CrossRef](#)]
54. Cattolica, R. OH rotational temperature from 2-line laser-excited fluorescence. *Appl. Opt.* **1981**, *20*, 1156–1166. [[CrossRef](#)]
55. Chen, H.; Hu, R.; Xie, P.; Xing, X.; Ling, L.; Li, Z.; Wang, F.; Wang, Y.; Liu, J.; Liu, W. A hydroxyl radical detection system using gas expansion and fast gating laser-induced fluorescence techniques. *J. Environ. Sci.* **2018**, *65*, 190–200. [[CrossRef](#)] [[PubMed](#)]
56. Copeland, C.; Friedman, J.; Rensizbulut, M. Planar temperature imaging using thermally assisted laser induced fluorescence of OH in a methane-air flame. *Exp. Therm. Fluid Sci.* **2007**, *31*, 221–236. [[CrossRef](#)] [[PubMed](#)]
57. Crosley, D.R.; Smith, G.P. Vibrational energy-transfer in laser-excited $A^2\Sigma^+$ OH as flame thermometer. *Appl. Opt.* **1980**, *19*, 517–520. [[CrossRef](#)]

58. Dilecce, G.; Martini, L.M.; Cepelli, M.; Scotoni, M.; Tosi, P. Progress on laser induced fluorescence in a collisional environment: The case of OH molecules in ns pulsed discharges. *Plasma Sources Sci. Technol.* **2019**, *28*, 025012. [[CrossRef](#)]
59. Dreizler, A.; Taday, R.; Monkhouse, P.; Wolfrum, J. Time and Spatially Resolved LIF of OH A $^2\Sigma^+$ ($v' = 1$) in Atmospheric-Pressure Flames using Picosecond Excitation. *Appl. Phys. B Photophys. Laser Chem.* **1993**, *57*, 85–87. [[CrossRef](#)]
60. Kienle, R.; Lee, M.P.; Kohse-Höinghaus, K. A scaling formalism for the representation of rotational energy transfer in OH (A (2)Sigma (+)) in combustion experiments. *Appl. Phys. B Lasers Opt.* **1996**, *63*, 403–418. [[CrossRef](#)]
61. Killinger, D.K.; Hanabusa, M. Intensity and pressure-dependence of resonance fluorescence of OH induced by a tunable uv laser. *Phys. Rev. A* **1976**, *13*, 2145–2152.
62. Kollner, M.; Monkhouse, P. Time-resolved LIF of OH in the flame front of premixed and diffusion flames at atmospheric pressure. *Appl. Phys. B Lasers Opt.* **1995**, *61*, 499–503. [[CrossRef](#)]
63. Mather, J.H.; Stevens, P.S.; Brune, W.H. OH and HO₂ measurements using laser-induced fluorescence. *J. Geophys. Res. Atmos.* **1997**, *102*, 6427–6436. [[CrossRef](#)]
64. Nielsen, T.; Bormann, F.; Burrows, M.; Andresen, P. Picosecond laser-induced fluorescence measurement of rotational energy transfer of OH A $^2\Sigma^+$ ($v' = 2$) in atmospheric pressure flames. *Appl. Opt.* **1997**, *36*, 7960–7969. [[CrossRef](#)]
65. Sappey, A.D.; Copeland, R.A. Laser double-resonance study of OH ($X^2\Pi_i, v = 12$). *J. Mol. Spectrosc.* **1990**, *143*, 160–168. [[CrossRef](#)] [[PubMed](#)]
66. Sick, V.; Wermuth, N. Single-shot imaging of OH radicals and simultaneous OH radical/acetone imaging with a tunable Nd:YAG laser. *Appl. Phys. B Lasers Opt.* **2004**, *79*, 139–143. [[CrossRef](#)]
67. Stone, D.; Whalley, L.K.; Ingham, T.; Edwards, P.M.; Cryer, D.R.; Brumby, C.A.; Seakins, P.W.; Heard, D.E. Measurement of OH reactivity by laser flash photolysis coupled with laser-induced fluorescence spectroscopy. *Atmos. Meas. Tech.* **2016**, *9*, 2827–2844. [[CrossRef](#)]
68. Zizak, G.; Lanauze, J.A.; Winefordner, J.D. An experimental study of the excited state rotational population of OH in flames using laser induced fluorescence. *Combust. Flame* **1986**, *65*, 203–214. [[CrossRef](#)]
69. Graña-Otero, J.; Mahmoudi, S. Excited OH kinetics and distribution in H₂ premixed flames. *Fuel* **2019**, *255*, 1115750. [[CrossRef](#)]
70. Greenslade, M.E.; Letser, M.I. (2+1) resonance-enhanced ionization spectroscopy of a state-selected beam of OH radicals. *J. Chem. Phys.* **2005**, *123*, 074309. [[CrossRef](#)]
71. Jeffries, J.B.; Kohse-Höinghaus, K.; Smith, G.P.; Copeland, R.A.; Crosley, D.R. Rotational-level-dependent quenching of OH (A $^2\Sigma^+$) at flame temperatures. *Chem. Phys. Lett.* **1988**, *152*, 160–166. [[CrossRef](#)]
72. Neuber, A.A.; Janicka, A.; Hassel, E.P. Thermally assisted fluorescence of laser-excited OH A $^2\Sigma^+$ as a flame diagnostic tool. *Appl. Opt.* **1996**, *35*, 4033–4040. [[CrossRef](#)]
73. Palmer, J.L.; Hanson, R.K. Temperature imaging in a supersonic free jet of combustion gases with two-line OH fluorescence. *Appl. Opt.* **1996**, *35*, 485–499. [[CrossRef](#)] [[PubMed](#)]
74. Smith, G.P.; Crosley, D.R. Vibrational-energy transfer in A $^2\Sigma^+$ OH in flames. *Appl. Opt.* **1983**, *22*, 1428–1430. [[CrossRef](#)] [[PubMed](#)]
75. Carlone, C.; Dalby, F.W. Spectrum of the hydroxyl radical. *Can. J. Phys.* **1969**, *47*, 1945–1957. [[CrossRef](#)]
76. Copeland, R.A.; Jeffries J.B.; Crosley, D.R. The OH A $^2\Sigma^+$ – X $^2\Pi_i(4, 2)$ band-line positions and linewidths. *J. Mol. Spectrosc.* **1990**, *143*, 183–185. [[CrossRef](#)]
77. Coxon, J.A.; Foster, S.C. Rotational analysis of hydroxyl vibration-rotation emission bands: Molecular constants for OH X $^2\Pi$, $6 \leq v \leq 10$. *Can. J. Phys.* **1980**, *60*, 41–48. [[CrossRef](#)]
78. Coxon, J.A.; Sappey, A.D.; Copeland, R.A. Molecular constants and term values for the hydroxyl radical, OH: The X $^2\Pi$ ($v=8,12$), A $^2\Sigma^+$ ($v=4-9$), B $^2\Sigma^+$ ($v=0,1$), and C $^2\Sigma^+$ ($v=0,1$) states. *J. Mol. Spectrosc.* **1991**, *145*, 41–55. [[CrossRef](#)]
79. Dieke, G.H.; Crosswhite, H.M. The ultraviolet bands of OH - fundamental data. *J. Quant. Spectrosc. Radiat. Transfer* **1962**, *2*, 97–199. [[CrossRef](#)]
80. Dyer, M.J.; Knutsen, K.; Copeland, R.A. Energy transfer in the ground state of OH: Measurements of OH ($v = 8, 10, 11$) removal. *J. Chem. Phys.* **1997**, *107*, 7809–7815. [[CrossRef](#)]
81. Gillis, J.R.; Goldman, A.; Stark, G.; Rinsland, C.P. Line parameters for the A $^2\Sigma^+$ – X $^2\Pi$ bands of OH. *J. Quant. Spectrosc. Radiat. Transfer* **2001**, *68*, 225–230. [[CrossRef](#)]

82. Hwang, E.S.; Lipson, J.B.; Field, R.W.; Dood, J.R. Detection of OH (X, v'', J'') via the $B^2\Sigma^+ - X^2\Pi$ transition and properties of the $B^2\Sigma^+$ state. *J. Phys. Chem. A* **2001**, *105*, 6030–6037. [[CrossRef](#)]
83. Langhoff, S.R.; Partridge, H. Theoretical-study of the lambda-doubling parameters for $X^2\Pi$ OH. *J. Mol. Spectros.* **1984**, *105*, 261–275. [[CrossRef](#)]
84. Langhoff, S.R.; Sink, M.L.; Pritchard, R.H.; Kern, C.W. Theoretical-study of the spin-orbit coupling in the $X^2\Pi$ state of OH. *J. Mol. Spectrosc.* **1982**, *96*, 200–218. [[CrossRef](#)]
85. Lengel, R.K.; Crosley, D.R. Rotational dependence of vibrational-relaxation in $A^2\Sigma^+$ OH. *Chem. Phys. Lett.* **1975**, *32*, 261–264. [[CrossRef](#)]
86. Lengel, R.K.; Crosley, D.R. Comments on “Electronic quenching and vibrational-relaxation of OH ($A^2\Sigma^+, v' = 1$) state”. *J. Chem. Phys.* **1976**, *64*, 3900–3901. [[CrossRef](#)]
87. Lengel, R.K.; Crosley, D.R. Energy-transfer in $^2\Sigma^+$ OH I. Rotational. *J. Chem. Phys.* **1977**, *67*, 2085–2101. [[CrossRef](#)]
88. Lengel, R.K.; Crosley, D.R. Energy-transfer in $^2\Sigma^+$ OH II. Vibrational. *J. Chem. Phys.* **1978**, *68*, 5309–5324. [[CrossRef](#)]
89. Levin, D. A.; Laux, C.O.; Kruger, C.H. A general model for the spectral calculation of OH radiation in the ultraviolet. *J. Quant. Spectrosc. Radiat. Transfer* **1999**, *61*, 377–392. [[CrossRef](#)]
90. Lucht, R.P.; Sweeney, D.W.; Laurendeau, N.M. Time-resolved fluorescence investigation of rotational transfer in $A^2\Sigma^+ (v = 0)$ OH. *Appl. Opt.* **1986**, *25*, 4086–4095. [[CrossRef](#)]
91. Raab, F.; Bergeman, T.; Lieberman, D.; Metcalf, H. Precision study of the $A^2\Sigma^+$ state of the OH radical. *Phys. Rev. A* **1981**, *24*, 3120–3135. [[CrossRef](#)]
92. Sechler, T.D.; Dempsey, L.O.; Lester, M.I. State-to-State Vibrational Energy Transfer in OH $A^2\Sigma^+$ with N_2 . *J. Phys. Chem. A* **2009**, *113*, 8845–8851. [[CrossRef](#)]
93. Steffens, K. L.; Crosley, D.R. Vibrational energy transfer in OH $A^2\Sigma^+$ between 195 and 295 K. *J. Chem. Phys.* **2000**, *112*, 9427–9432. [[CrossRef](#)] [[PubMed](#)]
94. Parigger, C.G.; Helstern, C.M.; Jordan, B.S.; Surmick, D.M.; Splinter, R. Laser-Plasma Spatiotemporal Cyanide Spectroscopy and Applications. *Molecules* **2020**, *25*, 615. [[CrossRef](#)]
95. Cremers, D.A.; Radziemski, L.J. *Handbook of Laser-Induced Breakdown Spectroscopy*; John Wiley & Sons Ltd.: New York, NY, USA, 2006. [[CrossRef](#)] [[PubMed](#)]
96. Singh, J.P.; Thakur, S.N. (Eds.) *Laser Induced Breakdown Spectroscopy*; Elsevier Science: New York, NY, USA, 2007.
97. Gautam, G.; Helstern, C.M.; Drake, K.A.; Parigger, C.G. Imaging of Laser-induced Plasma Expansion Dynamics in Ambient Air. *Int. Rev. At. Mol. Phys.* **2016**, *7*, 45–51.
98. Brieschenk, S.; O’Byrne, S.; Kleine, H. Visualization of jet development in laser-induced plasmas. *Opt. Lett.* **2013**, *38*, 664–666.
99. Harilal, S.S.; Miloshevsky, G.V.; Diwakar, K.; LaHaye, N.; Hassanein, A. Experimental and computational study of complex shockwave dynamics in laser ablation plumes in argon atmosphere. *Phys. Plasmas* **2012**, *19*, 083504. [[CrossRef](#)]
100. Gordon, S.; McBride, B. *Computer Program for Calculation of Complex Equilibrium Compositions, Rocket Performance, Incident and Reflected Shocks, and Chapman-Jouguet Detonations*; Interim Revision, NASA Report SP-273; NASA Lewis Research Center: Cleveland, OH, USA, 1976. [[CrossRef](#)]
101. McBride, B.J.; Gordon, S. Computer Program for Calculating and Fitting Thermodynamic Functions, NASA RP-1271, 1992; On-Line 2005 Version. Available online: <https://cearun.grc.nasa.gov/> (accessed on 14 December 2019).
102. Engineering Toolbox, Water Vapor in Air. Available online: https://www.engineeringtoolbox.com/water-vapor-air-d_854.html (accessed on 15 February 2020).
103. Engineering Toolbox, Air Composition. Available online: https://www.engineeringtoolbox.com/air-composition-d_212.html (accessed on 15 February 2020).
104. Kogelnik, H.; Li, T. Laser Beams and Resonators. *Appl. Opt.* **1966**, *5*, 1550–1567.
105. Technical Note: Gaussian Beam Optics. Available online: <https://www.newport.com/n/gaussian-beam-optics> (accessed on 15 February 2020). [[CrossRef](#)]
106. Parigger, C.G.; Helstern, C.M.; Gautam, G. Temporally and Spatially Resolved Emission Spectroscopy of Hydrogen, Cyanide and Carbon in Laser-Induced Plasma. *Atoms* **2019**, *7*, 74.

107. Guan, G. On the Analysis of Emission Spectra and Interference Images. Ph.D. Dissertation, University of Tennessee, Knoxville, TN, USA, 1998. [[CrossRef](#)]
108. Hornkohl, J.O. (University of Tennessee Space Institute, Tullahoma, TN 37388, USA). Personal communication, 1996.
109. Parigger, C.G.; Guan, G.; Hornkohl, J.O. Laser-induced breakdown spectroscopy: analysis of OH spectra. In *Laser Induced Plasma Spectroscopy and Applications*; Trends in Optics and Photonics Series; Optical Society of America: Washington, DC, USA, 2002; Volume 81, pp. 102–103.



© 2020 by the authors. Licensee MDPI, Basel, Switzerland. This article is an open access article distributed under the terms and conditions of the Creative Commons Attribution (CC BY) license (<http://creativecommons.org/licenses/by/4.0/>).